A mathematical model for co-registered data from electroencephalography and diffusive optical tomography

Marion Darbas, Stephanie Lohrengel, B Sulis

A mathematical model for co-registered data from electroencephalography and diffusive optical tomography

M. Darbas[1], S. Lohrengel[2], and B. Sulis[2]

[1]LAGA UMR CNRS 7539, Université Sorbonne Paris Nord, France
[2]LMR UMR CNRS 9008, Université de Reims-Champagne Ardenne, Reims, France

June 18, 2024

Abstract

A new mathematical model for co-registered time-dependent electroencephalography (EEG) and diffusive optical tomography (DOT) is developed and analysed. Evolution with time is introduced into the standard EEG model by considering time-dependent dipolar sources whereas time-dependent optical parameters yield the instationary DOT model. Dimensional analysis shows the validity of both the quasi-stationary approximation for EEG and the diffusion approximation with frequency-modulated source terms for DOT in all tissues of the humain head. A non-linear system of differential equations based on ionic currents is used to model the post-synaptic current and hemodynamic parameters at the neuron level which, in turn, provide the moment of the dipolar source term of the EEG boundary value problem and the behaviour in time of the optical parameters of the DOT model. The well-posedness of the time-dependent EEG problem is proved by the subtraction approach for moments with L^2-regularity in time and continuous source trajectories. For the time-dependent DOT model with continuous optical parameters in time, standard results of functional analysis apply. We explain the full pipeline from the input current of stimulation up to the measurements recorded at the electroptodes. Numerical results for a three-dimensional realistic head model of a neonate illustrate the capacity of simultanous EEG/DOT measurements to attest neurovascular coupling between the neural activity and changes in the hemodynamic parameters.

Keywords: time-dependent electroencephalography, time-dependent diffusive optical tomography, dipolar sources, neurovascular coupling, neuronal model.

Mathematics Subject Classification: 92C50, 92-10, 65N30.

Contents

Introduction

The challenges of understanding the human brain are major and of great interest to better diagnosis and cure of many brain diseases. Various brain imaging modalities have been developed over the years, each dedicated to the investigation of some specific brain functions. We can cite functional magnetic resonance imaging (fMRI), computerized tomography (CT), positron emission tomography (PET), electroencephalography (EEG), magnetoencephalography (MEG), functional near-infrared spectroscopy (fNIRS) or diffuse optical tomography (DOT). Some of them provide complementary information on the brain and its disorders, and the benefits of multimodal neuroimaging are studied in the last decades. In this paper, we focus on the synchronous measurements of EEG and DOT.

On the one hand, electroencephalography (EEG) is one of the most widespread functional brain imaging techniques. Measurements of the electric potential generated by normal or pathological brain activity are taken at electrodes attached to the scalp. They record in a passive and non-invasive way the voltage potential fluctuations between different cortical regions. EEG-monitoring can be done at the bedside of the patient which makes the technique particularly appropriate for neonates and premature babies. The important goal of brain imaging using EEG is to localize cerebral sources generating measured EEG signals. EEG is known to have an excellent temporal resolution and is able to record neural events in order of one millisecond. Its spatial resolution is generally limited (a few centimeters). Neonatal EEG is used to assess seizure recognition and classification and to make epilepsy syndrome diagnosis (e.g [35]). It provides also prognostic information for other brain dysfunctions (e.g [24]).

On the other hand, diffuse optical tomography (DOT) is a functional brain imaging technique that measures at optodes (sensors) on the scalp the hemodynamic changes in the brain. DOT is an extension of fNIRS (see e.g [25]). More precisely, DOT aims in localizing changes in oxy- and deoxyhemoglobin (that result from brain activity) within the brain by using absorption of near-infrared light. Similar to EEG, it is a non-invasive technique. DOT may be seen as an alternative to fMRI. In comparison to fMRI, the DOT system has the advantage to be relatively low-cost, portable and bedside-compatible.

The development of multimodal analysis yields a more detailed understanding of brain dynamics. We are particularly interested in the coupling of EEG with optical imaging, taking advantage of the possible coregistration of EEG and NIRS which has already been operated by collaborators from GRAMFC INSERM UMR-S 1105 (Amiens' hospital) [31] for neonates and premature babies. EEG measures directly neuronal activity while optical imaging techniques (DOT, NIRS, fNIRS) capture the physiological changes linked to neurovascular coupling. To sum up, in response to a certain task (due to normal or pathological origin), the neural activity increases in a brain area. A metabolic demand, i.e. changes in oxy- and deoxyhemoglobin, is observed generally in that area. Co-registered data from EEG and DOT give information to clinicians for understanding the neurovascular coupling which occurs in some brain disorders. The coupling of the two modalities is more particularly used in pediatric clinical research [42, 17]. An example is the study

of [37] where hemodynamic changes have been observed among 10s before an epileptic seizure. Another clinical investigation using simultaneous EEG and DOT is addressed in [9].

The mathematical modelling of EEG and DOT has been widely addressed in the literature. Without being exhaustive, we cite [41, 33, 43, 10] and references therein for an analysis of the forward EEG problem and [1, 2, 22] for an overwiew of models for DOT based on the diffusion approximation. The aforementioned models are static or time-harmonic with time-independent parameters and source terms. Time-resolved DOT is an existing imaging modality [30] that is actually less relevant for clinical purposes due to the high cost of the technical device. In this paper, we thus limit our investigations for DOT with frequency modulated source terms.

The present work is dedicated to the development and the analysis of a mathematical model for simulating co-registered time-dependent EEG-DOT data. Given an input stimulus in the brain, the underlying forward problem consists in computing the electric potential and the photon density which are generated by the brain activity, corresponding to the stimulus, at electroptodes on the scalp. This requires to model the neurovascular coupling mechanism, that is the dynamics of the neural activity and its vascular response. Different models based on systems of non-linear ordinary differential equations have been developed (see e.g. [3, 7, 8, 28, 29, 39] and references therein). We focus on a model for neuronal activity based on the work of [29] coupled to the balloon model [7, 8] for the hemodynamic response. In a first step, we use these models to get the time-dependent postsynaptic current and hemodynamic parameters at the neuron level. With this local brain information in hand, we propose a space–time modeling for co-registered EEG/DOT data, requiring PDE-based models. To this end, we introduce the time evolution in the standard instationary forward models for EEG and DOT.

The paper is organized as follows. In Section 1, we derive a time-dependent model for the EEG forward problem and we address an existence and uniqueness result using the subtraction method. In Section 2, in the same way as for EEG, we propose a model for the diffusion approximation with time-dependent optical parameters in a frequency-modulated setting. Section 3 is devoted to the modeling of the neurovascular coupling. Finally, numerical simulations of co-registered EEG/DOT measurements for a realistic three-dimensional head model are performed in Section 4.

1 A mathematical model for time-dependent EEG

1.1 Dimensional analysis of Maxwell's equations

We study an electromagnetic phenomenon in a space-time domain with characteristic length ℓ and time scale τ. The continuous medium is characterized by its electric permittivity ε, magnetic permeability μ and conductivity σ. Maxwell's equations describe the propagation of an electromagnetic field in this medium. Under the assumption that the constitution laws of the medium are linear, they are given by

$$\begin{aligned} &\nabla \cdot \mathbf{B} = 0, && \nabla \times \mathbf{B} = \mu(\varepsilon \partial_t \mathbf{E} + \mathbf{J}), \\ &\nabla \times \mathbf{E} = -\partial_t \mathbf{B}, && \nabla \cdot \mathbf{E} = \frac{\rho}{\varepsilon}, \end{aligned} \tag{1}$$

and model the interaction between the electric field $\mathbf{E}$, the magnetic induction $\mathbf{B}$, the charge density ρ and the current density $\mathbf{J}$. In a conducting medium with conductivity σ, Ohm's law states that the free current density is given by $\mathbf{J} = \sigma \mathbf{E}$. In the presence of impressed current sources, a source term $\mathbf{j}^p$ should be added to $\mathbf{J}$.

The static limit of Maxwell's equations is well understood in the case where all fields and sources are time-independent. As soon as there is some time-dependence, however, the full Maxwell system should apply unless mathematical analysis shows that some terms can be neglected. EEG measures the cerebral activity during the observation. This activity is

clearly variable in time, meaning that time-dependent source terms should be considered. In this context, dimensional analysis is an interesting tool to reduce the set of Maxwell's equations and get simplified models under particular hypotheses. The idea is to observe the different physical quantities in terms of their units or dimensions. Smallness of some of them allows to neglect certain coupling between electric and magnetic fields [34]. To this end, we introduce the velocity of the system with modulus $v = \ell/\tau$. The light celerity in the medium with electromagnetic parameters ε and μ is given by $c = 1/\sqrt{\varepsilon\mu}$. Here, we are interested in limit configurations where $v \ll c$.

For going further into details in the analysis, a first step is to express the quantities ℓ and c in terms of the electromagnetic parameters ε, μ and σ. Following [34], we introduce the quantity $\tau_e = \varepsilon/\sigma$ which has dimension of time and can be interpreted as the electric charge diffusion time. Similarly, the quantity $\ell c\mu\sigma$ can be shown to be dimensionless and can be written as the quotient of $\tau_m = \mu\sigma\ell^2$ and $\tau_{em} = \ell/c$ which both have dimension of time. We next proceed to the scaling of Maxwell's equations. To this end, set $\mathbf{E}(t,\mathbf{x}) = e\mathbf{E}'(t',\mathbf{x}')$ and $\mathbf{B}(t,\mathbf{x}) = b\mathbf{B}'(t',\mathbf{x}')$ where e, b are reference quantities and $\mathbf{E}'$, $\mathbf{B}'$ are dimensionless quantities of order $\mathcal{O}(1)$ depending on $t' = t/\tau$ and $\mathbf{x}' = \mathbf{x}/\ell$. In the sequel, prime notation corresponds to dimensionless operators or variables.

Using the definition of the characteristic times, Faraday's and Ampère's laws $\nabla\times\mathbf{E} = -\partial_t\mathbf{B}$ and $\nabla\times\mathbf{B} = \mu(\varepsilon\partial_t\mathbf{E} + \sigma\mathbf{E})$ become respectively

$$\nabla'\times\mathbf{E}' = -\frac{\tau_{em}}{\tau}\frac{cb}{e}\partial_{t'}\mathbf{B}', \tag{2}$$

and

$$\nabla'\times\mathbf{B}' = \frac{\tau_{em}}{\tau}\frac{e}{cb}\partial_{t'}\mathbf{E}' + \frac{\tau_{em}}{\tau_e}\frac{e}{cb}\mathbf{E}'. \tag{3}$$

We are interested in the low frequency range where the characteristic dimensions of the system are such that

$$\tau_{em} \ll \tau,\ \tau_e \ll \tau,\ \text{and}\ \tau_m \ll \tau. \tag{4}$$

Then, we cannot have simultaneously $\dfrac{\tau_{em}}{\tau}\dfrac{cb}{e} = \mathcal{O}(1)$ and $\dfrac{\tau_{em}}{\tau}\dfrac{e}{cb} = \mathcal{O}(1)$ and at least one of the time derivatives in (2) or (3) has to be neglected. We aim to determine the limit model from the only order between the characteristic time scales.

One may notice that $\tau_{em}^2 = \tau_e\tau_m$ which amounts to saying that any order between τ_{em} and τ_e induces an order of τ_m with respect to τ_{em}. We distinguish three cases: $\tau_{em} \ll \tau_e$, $\tau_e \ll \tau_{em}$ and $\tau_e \sim \tau_{em}$. We choose to only detail the first one. According to assumption (4) on τ_e, the relation $\tau_{em} \ll \tau_e$ implies the order $\tau_m \ll \tau_{em} \ll \tau_e \ll \tau$. From $\tau_e \ll \tau$, we deduce that $\dfrac{\tau_{em}}{\tau} \ll \dfrac{\tau_{em}}{\tau_e}$. The displacement current in the right hand side of (3) can thus be neglected and we get

$$\nabla\times\mathbf{B} = \mu\mathbf{J}. \tag{5}$$

Since the left hand side of (3) is of order 1, we further have $\dfrac{cb}{e} \sim \dfrac{\tau_{em}}{\tau_e} \ll 1$. Hence, the right hand side in (2) can be neglected, too, which yields

$$\nabla\times\mathbf{E} = 0. \tag{6}$$

The cases $\tau_e \ll \tau_{em}$ and $\tau_e \sim \tau_{em}$ lead to the same conclusions. Thus, in a frequency range satisfying (4), we get the following approximation of Maxwell's equations

$$\begin{aligned} &\nabla\cdot\mathbf{B} = 0, && \nabla\times\mathbf{B} = \mu\mathbf{J},\\ &\nabla\times\mathbf{E} = 0, && \nabla\cdot\mathbf{E} = \frac{\rho}{\varepsilon}, \end{aligned} \tag{7}$$

called the quasi-stationary model.

1.2 Quasi-stationary approximation for EEG with time-dependent sources

In this section, we compare the order of magnitude of the characteristic times for the electromagnetic parameters of the different head tissues. In mathematical modeling of brain activity, one assumes that the magnetic permeability of head tissues is close to the one of free space. The parameters of the medium are given by $\varepsilon = \varepsilon_r \varepsilon_0$ and $\mu = \mu_0$ where $\varepsilon_0 = 8.85 \times 10^{-12}\text{F.m}^{-1}$ and $\mu_0 = 4\pi \times 10^{-7}\text{H.m}^{-1}$ are respective vacuum permittivity and permeability. The relative permittivity ε_r and the conductivity σ depend on the tissue, but also on the frequency range. The typical frequency range of the electromagnetic fields in the head is inferior to 100 Hz [15] and we thus take $\tau \approx 0.01$s as the characteristic time scale. We consider a multilayer head model which distinguishes between white and grey matter and takes into account the cerebrospinal fluid (CSF) as well as skull and scalp. Uncertainty about the electric parameters should be taken into account since *in vivo* measurements in the human body are in general not available, especially for neonates and premature babies. In Table 1, we take the values for the electric permittivity from the IT'IS data base [21] which are given for a specific frequency from a parametrization fit based on the dispersion relation owing to [16]. The conductivity values are taken from [26, 5] for neonates. We recall the formulæ for the three characteristic times

$$\tau_e = \varepsilon/\sigma, \tau_m = \mu\sigma\ell^2, \tau_{em} = \sqrt{\tau_e \tau_m}.$$

The characteristic length scale ℓ should be given by the thickness of the tissue in consideration. Notice, however, that τ_e is independent from the characteristic length ℓ whereas $\tau_m \sim \ell^2$ and $\tau_{em} \sim \ell$. Hence, if the quasi-static approximation is valid for a given ℓ, it is also valid for any smaller length scale. We thus take for ℓ the dimensions of the neonatal head, i.e. $\ell \approx 0.12$ m. We then deduce the values of the three characteristic times.

	White matter	Grey matter	CSF	Skull	Scalp
ε_r	1.67×10^6	3.91×10^6	1.1×10^2	5.85×10^3	1.14×10^3
σ [S/m]	0.14	0.33	1.8	0.04	0.33
τ_m [s]	2.53×10^{-9}	5.97×10^{-9}	3.25×10^{-8}	7.2×10^{-10}	6.0×10^{-9}
τ_{em} [s]	5×10^{-7}	8×10^{-7}	4.19×10^{-9}	3.1×10^{-8}	1.35×10^{-8}
τ_e [s]	1.05×10^{-5}	1.05×10^{-4}	5.4×10^{-10}	1.3×10^{-6}	3.1×10^{-8}

Table 1: Electric parameter set at 100 Hz [21, 26] and characteristic times.

From Table 1, we infer $\tau_m \ll \tau_{em} \ll \tau_e \ll \tau$ for white matter, grey matter and skull. In CSF, the order is reversed and in the scalp, the three characteristic times are approximately of the same order with $\tau_m \sim \tau_{em} \sim \tau_e \ll \tau$. These situations correspond to the different cases studied in the previous dimensional analysis. Thus, for modeling EEG, the quasi-stationary approximation (7) of the full Maxwell equations can be considered as a valid model. We focus on values for neonates and premature babies, but the conclusions of the dimensional analysis hold true for adults as well, the main difference being in the value of σ in the skull which is generally assumed to be ten times smaller than in neonates.

Equation $\nabla \times \mathbf{E} = 0$ shows that the electric field $\mathbf{E}$ derives from a scalar electric potential, denoted by u, and is written as

$$\mathbf{E}(t, \mathbf{x}) = -\nabla u(t, \mathbf{x}), \ (t, \mathbf{x}) \in (0, T) \times \Omega, \tag{8}$$

with $T > 0$ an observation time and $\Omega \subset \mathbb{R}^d$ $(d = 2, 3)$ a head model. In the brain and in particular in the cortex, the synchronized effect among a multitude of neurons creates an intracellular current denoted by $\mathbf{j}^p$. The current density $\mathbf{J}$ produced by cerebral activity thus splits into two terms

$$\mathbf{J} = \sigma\mathbf{E} + \mathbf{j}^p. \tag{9}$$

By replacing (8) and (9) in the equation $\nabla \times \mathbf{B} = \mu \mathbf{J}$, and by applying the divergence operator, we obtain

$$0 = \nabla \cdot (\nabla \times \mathbf{B}) = \mu \nabla \cdot (\mathbf{j}^p - \sigma \nabla u), \tag{10}$$

which gives the following elliptic equation

$$\nabla \cdot (\sigma \nabla u) = \nabla \cdot \mathbf{j}^p. \tag{11}$$

In order to numerically reproduce spatially localized phenomena which are variable in time, we propose a time-dependent model for the source term $\mathbf{j}^p$ in the form of a set of M electric dipoles located in the brain

$$\mathbf{j}^p(t, \cdot) = \sum_{m=1}^{M} \mathbf{q}_m(t) \delta(\cdot - S_m(t)). \tag{12}$$

Here, $S_m(t) \in \Omega$ and $\mathbf{q}_m(t) \in \mathbb{R}^d$ are, respectively, the position and the moment of the m-th source at time t which is situated in the subdomain of Ω that models the brain or, more precisely, the grey matter. The right hand side of (11) then reads

$$F(t, \cdot) := \nabla \cdot \mathbf{j}^p(t, \cdot) = \sum_{m=1}^{M} \mathbf{q}_m(t) \cdot \nabla \delta(\cdot - S_m(t)). \tag{13}$$

Assuming that the conductivity of air is zero and that no electric current can flow out of the scalp, the electric potential u is then solution of the following boundary problem with homogeneous Neumann condition

$$\begin{cases} \nabla \cdot (\sigma \nabla u) = F & \text{in } (0,T) \times \Omega, \\ \sigma \partial_{\boldsymbol{n}} u = 0 & \text{on } (0,T) \times \partial\Omega. \end{cases} \tag{14}$$

1.3 The subtraction approach for EEG with time-dependent sources

In this section, we address the resolution of the forward problem (14). Mathematically, a head model can be described as follows. Let $\Omega \subset \mathbb{R}^d$ be a bounded simply connected domain with regular boundary $\Gamma := \partial\Omega$ and consider a partition of Ω into P open subdomains $(\Omega_p)_{p=1,\dots,P}$, such that

$$\bar{\Omega} = \bigcup_{p=1}^{P} \bar{\Omega}_p \text{ and } \Omega_p \cap \Omega_q = \emptyset \ \forall p \neq q.$$

Subdomains Ω_p describe the different tissues of the head. In the case of concentric subdomains as in Figure 1, we denote by Γ_p the interface between the subdomains Ω_p and Ω_{p+1} and assume that $(\Gamma_p)_p$ are closed regular surfaces. Let $\mathbf{n}_p$ be the unit normal vector to Γ_p from Ω_p to Ω_{p+1}.

Notice that (14) includes the following transmission conditions at any interface Γ_p between two subdomains Ω_p and Ω_q

$$[u]_{|\Gamma_p} = [\sigma \partial_{\boldsymbol{n}} u]_{|\Gamma_p} = 0 \text{ on } (0,T) \times \Gamma_p. \tag{15}$$

Here, $[f]_{|\Gamma_p} = f_{|\Omega_q} - f_{|\Omega_p}$ denotes the jump across the interface Γ_p of the function f defined on Ω.

We make the following assumptions on the moments, sources, and the conductivity:

(H_1) $\mathbf{q}_m \in L^2(0,T)^d$ and $S_m \in \mathcal{C}^0([0,T])^d$, $\forall m \in \{1, \dots, M\}$.

(H_2) At time t, the points $(S_m(t))_m$ are mutually distinct, i.e. $S_m(t) \neq S_k(t), \forall m \neq k$.

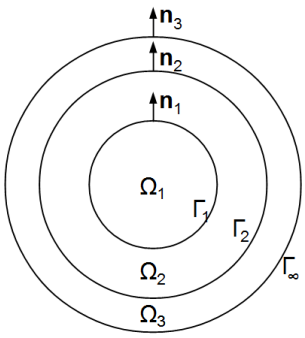

Figure 1: Three-layer head model

(H_3) All sources are located in the same subdomain Ω_{p_0}, $p_0 \in \{1, \dots, P\}$, and there is a domain $D \subset\subset \Omega_{p_0}$, such that

$$\bigcup_{m=1}^{M} \{S_m(t),\ t \in [0,T]\} \subset D, \tag{16}$$

and the conductivity is constant on D: $\sigma_{|D} = \sigma_D$ for a constant $\sigma_D > 0$.

Due to the lack of regularity of the source term F, a direct variational formulation of (14) in $H^1(\Omega)$ is not possible. A possibility is to apply the subtraction approach [14, 6, 43]. It consists of decomposing the potential u into a potential $\tilde{u}$ which contains the singularity and a regular lifting w:

$$u = \tilde{u} + w \text{ on } (0,T) \times \Omega.$$

But in the time-dependent setting with moments $\mathbf{q}_m$ belonging to $L^2(0,T)^d$, the boundary value problem (14) with source term (13) can not be understood at fixed time t. The definition of the singular portential $\tilde{u}$ thus needs to be done with caution. To this end, we introduce for $m \in \{1, \dots, M\}$ and $i \in \{1, \dots, d\}$, the *canonical source term* $F_m^{(i)}$:

$$\forall t \in [0,T],\ F_m^{(i)}(t,\cdot) = \mathbf{e}^{(i)} \cdot \nabla \delta(\cdot - S_m(t)) \tag{17}$$

where $\mathbf{e}^{(i)}$ denotes the i-th canonical basis vector of $\mathbb{R}^d$. Notice that $F_m^{(i)}$ is well defined at any time step t since S_m is continuous on $[0,T]$. The associated singular potential $\tilde{u}_m^{(i)}(t,\cdot)$, $i = 1, \dots, d$, is solution of the following Poisson equation

$$\forall t \in [0,T],\ \sigma_D \Delta \tilde{u}_m^{(i)}(t,\cdot) = F_m^{(i)}(t,\cdot) \text{ in } \mathbb{R}^d.$$

Thus, $\tilde{u}_m^{(i)}(t,\cdot)$ is obtained by convolution in the space variable $\mathbf{x}$ of the fundamental solution of the Laplace equation with the right hand side $\dfrac{1}{\sigma_D}\mathbf{e}^{(i)} \cdot \nabla \delta(\cdot - S_m(t))$ which leads to

$$\tilde{u}_m^{(i)}(t,\mathbf{x}) = \frac{1}{2^{d-1}\pi\sigma_D}\mathbf{e}^{(i)} \cdot \frac{\mathbf{x} - S_m(t)}{|\mathbf{x} - S_m(t)|^d},\ \forall t \in [0,T],\ \forall \mathbf{x} \in \mathbb{R}^d \setminus \{S_m(t)\}. \tag{18}$$

At fixed time $t \in [0,T]$, consider the following boundary value problem with regular right hand side

$$\begin{cases} -\nabla \cdot (\sigma \nabla w_m^{(i)}(t,\cdot)) = \nabla \cdot ((\sigma - \sigma_D)\nabla \tilde{u}_m^{(i)}(t,\cdot)) & \text{in } \Omega, \\ \sigma \partial_{\boldsymbol{n}} w_m^{(i)}(t,\cdot) = -\sigma \partial_{\boldsymbol{n}} \tilde{u}_m^{(i)}(t,\cdot) & \text{on } \Gamma. \end{cases} \tag{19}$$

We prove here below that (19) admits a variational solution in an appropriated vector space. To this end, define the bilinear form $a(\cdot,\cdot)$ on $H^1(\Omega) \times H^1(\Omega)$ by

$$a(w,v) = \int_\Omega \sigma \nabla w \cdot \nabla v \, \mathrm{d}\mathbf{x}.$$

For fixed $t \in [0,T]$, denote by $l_m^{(i)}(t;\cdot)$ the following linear form defined for $v \in H^1(\Omega)$,

$$l_m^{(i)}(t;v) = \int_{\Omega\setminus\bar{D}} (\sigma_D - \sigma)\nabla\tilde{u}_m^{(i)}(t,\cdot)\cdot\nabla v \,\mathrm{d}\mathbf{x} - \int_\Gamma \sigma_D \partial_{\boldsymbol{n}}\tilde{u}_m^{(i)}(t,\cdot)v \,\mathrm{d}s.$$

Since problem (19) involves a Neumann boundary condition, its solution is determined up to an additive constant only. We therefore introduce the subspace of $H^1(\Omega)$ of functions with vanishing mean value,

$$V = H^1(\Omega) \cap L_0^2(\Omega), \tag{20}$$

where

$$L_0^2(\Omega) = \left\{ v \in L^2(\Omega) \,\middle|\, \int_\Omega v \,\mathrm{d}\mathbf{x} = 0 \right\}.$$

Then, the following proposition holds true:

Proposition 1.1. *Let $\sigma \in L^\infty(\Omega)$ be such that $0 < \sigma_{\min} \le \sigma \le \sigma_{\max}$ a.e. on Ω with constants $\sigma_{\min}$ and $\sigma_{\max}$. Let $S_m \in \mathcal{C}^0(0,T)^d$ for any $m \in \{1,\dots,M\}$ and assume that (H_2) and (H_3) are satisfied. Then, for $m \in \{1,\dots,M\}$ and $i \in \{1,\dots,d\}$, the following problem admits a unique solution:*

$$\begin{cases} \text{Find } w_m^{(i)} \in \mathcal{C}^0([0,T];V) \text{ such that} \\ a(w_m^{(i)}(t,\cdot),v) = l_m^{(i)}(t;v) \quad \forall v \in H^1(\Omega),\ \forall t \in [0,T]. \end{cases} \tag{21}$$

The solution of (21) satisfies (19) in a weak sense.

Proof. According to the assumptions on σ, the bilinear form $a(\cdot,\cdot)$ is continuous and coercive on $V \times V$. For the linear form, consider $v \in H^1(\Omega)$ and $t \in [0,T]$. Since the potential $\tilde{u}_m^{(i)}(t,\cdot)$ is regular outside the domain D, we conclude that $l_m^{(i)}(t;\cdot)$ is continuous on $H^1(\Omega)$ and satisfies

$$|l_m^{(i)}(t;v)| \le C\|v\|_{H^1(\Omega)}$$

with a constant

$$C = 2\|\sigma\|_{L^\infty(\Omega)} \max_{t\in[0,T]} \|\nabla\tilde{u}_m^{(i)}(t,\cdot)\|_{L^2(\Omega\setminus\bar{D})} + C_\Gamma\sigma_D \max_{t\in[0,T]} \|\partial_{\boldsymbol{n}}\tilde{u}_m^{(i)}(t,\cdot)\|_{L^2(\Gamma)}$$

which is independent from t, where $C_\Gamma > 0$ is the constant of the trace operator on $H^1(\Omega)$. The compatibility condition $l_m^{(i)}(t;1) = 0$ can be proved as in [6] with the help of the solid angle formula. Then, Lax-Milgram's theorem guarantees existence and uniqueness of the solution at fixed time t. Now, notice that $\tilde{u}_m^{(i)}$ is continuous with respect to time on $\Omega \setminus D$ and $l_m^{(i)}$ depends continuously on $u_m^{(i)}$. This proves that $w_m^{(i)} \in \mathcal{C}^0([0,T];V)$ and we get

$$\|w_m^{(i)}(t,\cdot)\|_V \le \frac{C}{\alpha} \ \forall t \in [0,T]$$

where $\alpha > 0$ is the coercivity constant of $a(\cdot,\cdot)$. □

Now, the time-dependent EEG problem (14) with source term (13) admits a solution in the following sense:

Theorem 1.2. *Let $\sigma \in L^\infty(\Omega)$ be such that $0 < \sigma_{\min} \le \sigma \le \sigma_{\max}$ a.e. on Ω with constants $\sigma_{\min}$ and $\sigma_{\max}$. Assume (H_1) – (H_3) to be true. For $i \in \{1,\dots,d\}$ and $m \in \{1,\dots,M\}$, let $w_m^{(i)}$ be the solution of (21) where $\tilde{u}_m^{(i)}$ is defined by (18). Finally, denote by $q_m^{(i)}$ the i-th component of the moment $\mathbf{q}_m \in L^2(0,T)^d$. Then,*

$$u = \sum_{m=1}^{M}\sum_{i=1}^{d} q_m^{(i)}(\tilde{u}_m^{(i)} + w_m^{(i)}) \tag{22}$$

is solution of the time-dependent EEG problem

$$\begin{cases} \nabla \cdot (\sigma \nabla u) = F & \text{in } (0,T) \times \Omega, \\ \sigma \partial_{\boldsymbol{n}} u = 0 & \text{on } (0,T) \times \Gamma, \end{cases}$$

with source term

$$F(t,\cdot) = \sum_{m=1}^{M} \mathbf{q}_m(t) \cdot \nabla \delta(\cdot - S_m(t)).$$

Proof. In order to prove that the potential u under the form (22) is solution to problem (14), it is sufficient to notice that $\nabla \cdot (\sigma \nabla(\tilde{u}_m^{(i)} + w_m^{(i)}))$ is well defined at any time t since

$$\nabla \cdot (\sigma \nabla(\tilde{u}_m^{(i)} + w_m^{(i)})) = \nabla \cdot ((\sigma - \sigma_D)\nabla \tilde{u}_m^{(i)}) + \sigma_D \Delta \tilde{u}_m^{(i)} + \nabla \cdot (\sigma \nabla w_m^{(i)}) = F_m^{(i)}.$$

We further have $\sigma \partial_{\boldsymbol{n}}(\tilde{u}_m^{(i)} + w_m^{(i)}) = 0$ on $[0,T] \times \Gamma$ by construction.

□

2 Diffusive optical tomography with time-dependent coefficients

2.1 Dimensional analysis of the P1-approximation of the radiative transfer equation

Light propagation is mainly governed by absorption and scattering phenomena. A popular model for photon transport in a context where the wavelength in the near infrared range is small (750-900 nm) compared to the characteristic length of the human head, is the radiative transfer equation (RTE).

Let $\mathbb{S}$ be the unit sphere in $\mathbb{R}^3$ and denote by f a given phase function which describes the probability that a photon arriving from direction $\mathbf{s}$, is scattered in direction $\mathbf{s}'$. We assume that f depends only from the angle between $\mathbf{s}$ and $\mathbf{s}'$ which is the case in an isotropic medium, and is such that

$$\int_{\mathbb{S}} f(\mathbf{s} \cdot \mathbf{s}')\, d\mathbf{s}' = 1.$$

The unknown of the RTE is the specific intensity of light $I(t, \mathbf{x}, \mathbf{s})$ which depends on time t, position $\mathbf{x}$ and the direction $\mathbf{s}$. Let q be a light source. Then the RTE reads

$$\frac{1}{c}\partial_t I(t,\mathbf{x},\mathbf{s}) + \mathbf{s} \cdot \nabla I(t,\mathbf{x},\mathbf{s}) + \mu_t I(t,\mathbf{x},\mathbf{s}) = \mu_s \int_{\mathbb{S}} f(\mathbf{s} \cdot \mathbf{s}') I(t,\mathbf{x},\mathbf{s}')\, d\mathbf{s}' + q(t,\mathbf{x},\mathbf{s}). \quad (23)$$

Here, $\mu_t = \mu_a + \mu_s$ is the total attenuation coefficient depending on the absorption coefficient μ_a and the scattering coefficient μ_s in the biological tissue, and c is the speed of light in the medium.

Since the numerical resolution of the RTE results in a high computational cost, especially in the context of medical imaging applications, a common choice is to use the diffusion equation as an approximation. We will discuss here how to deal with time-dependent optical parameters. To this end, we define respectively, the diffuse photon density ϕ and the diffuse photon flux $\mathcal{J}$ by

$$\phi(t,\mathbf{x}) = \int_{\mathbb{S}} I(t,\mathbf{x},\mathbf{s})\, d\mathbf{s}, \quad (24)$$

and

$$\mathcal{I}(t,\mathbf{x}) = \int_{\mathbb{S}} I(t,\mathbf{x},\mathbf{s})\mathbf{s}\, d\mathbf{s}. \quad (25)$$

We further assume that the source term q is isotropic, i.e. $q = q(t, \mathbf{x})$. Expansion of the intensity I in terms of spherical harmonics up to the first order then yields the following system

$$\begin{aligned} \frac{1}{c}\partial_t \phi(t,\mathbf{x}) + \nabla \cdot \mathcal{I}(t,\mathbf{x}) + \mu_a(t,\mathbf{x})\phi(t,\mathbf{x}) &= q \qquad (26) \\ \frac{1}{c}\partial_t \mathcal{I}(t,\mathbf{x}) + \frac{1}{3}\nabla\phi(t,\mathbf{x}) + (\mu_a(t,\mathbf{x}) + \mu_s'(t,\mathbf{x}))\mathcal{I}(t,\mathbf{x}) &= 0, \qquad (27) \end{aligned}$$

where $\mu_s' = (1-g)\mu_s$ is the reduced scattering coefficient and g is the anisotropy factor. Now, consider a time-harmonic source term $q(t, \mathbf{x}) = q_0(\mathbf{x}) \exp(i\omega t)$ oscillating at a given pulsation $\omega > 0$. Since the optical parameters μ_a and μ_s' depend both on the time and the space variable, we cannot assume any more that the unknowns ϕ and $\mathcal{I}$ are separated in time and space. Let $\Phi(t, \mathbf{x})$ and $\mathbf{I}(t, \mathbf{x})$ be such that

$$\begin{aligned} \phi(t,\mathbf{x}) &= \Re\left(\Phi(t,\mathbf{x})\exp(i\omega t)\right), \\ \mathcal{I}(t,\mathbf{x}) &= \Re\left(\mathbf{I}(t,\mathbf{x})\exp(i\omega t)\right), \end{aligned}$$

where Φ and $\mathbf{I}$ are complex-valued functions of time and space. System (26)–(27) then reads

$$\begin{aligned} \frac{i\omega}{c}\Phi(t,\mathbf{x}) + \frac{1}{c}\partial_t\Phi(t,\mathbf{x}) + \nabla\cdot\mathbf{I}(t,\mathbf{x}) + \mu_a(t,\mathbf{x})\Phi(t,\mathbf{x}) &= q_0(\mathbf{x}) \qquad (28) \\ \frac{i\omega}{c}\mathbf{I}(t,\mathbf{x}) + \frac{1}{c}\partial_t\mathbf{I}(t,\mathbf{x}) + \frac{1}{3}\nabla\Phi(t,\mathbf{x}) + (\mu_a(t,\mathbf{x}) + \mu_s'(t,\mathbf{x}))\mathbf{I}(t,\mathbf{x}) &= 0. \qquad (29) \end{aligned}$$

In the same way as for the time-dependent EEG problem, we now proceed to the scaling of system (28)–(29). Let τ and ℓ be the characteristic time scale and length of the problem. Let further $\Phi(t, \mathbf{x}) = \varphi\mathcal{P}'(t', \mathbf{x}')$ and $\mathbf{I}(t, \mathbf{x}) = j\mathcal{I}'(t', \mathbf{x}')$ where φ and j are reference quantities and $\mathcal{P}'$ and $\mathcal{I}'$ are dimensionless of order $\mathcal{O}(1)$ depending on $t' = t/\tau$ and $\mathbf{x}' = \mathbf{x}/\ell$. As before, prime notation corresponds to dimensionless operators or variables and system (28)–(29) becomes

$$\begin{aligned} \frac{i\omega}{c}\varphi\mathcal{P}' + \frac{1}{c\tau}\varphi\partial_{t'}\mathcal{P}' + \frac{j}{\ell}\nabla'\cdot\mathcal{I}' + \mu_a\varphi\mathcal{P}' &= q_0, \qquad (30) \\ \frac{i\omega}{c}j\mathcal{I}' + \frac{1}{c\tau}j\partial_{t'}\mathcal{I}' + \frac{1}{3\ell}\varphi\nabla'\mathcal{P}' + (\mu_a + \mu_s')j\mathcal{I}' &= 0. \qquad (31) \end{aligned}$$

Now, we take into account that diffuse optical tomography operates in the time-harmonic setting at a frequency of $f = 10^8[Hz]$. According to [36, 37], oscillations in the concentrations of oxy- and deoxyhemoglobine occur at a frequency from 0.05 to $0.1[Hz]$. We thus have $\frac{1}{\tau} \ll \omega = 2\pi f$. Consequently, the second term in (30) (resp. (31)) is much smaller compared to the first term and we conclude that the time derivatives can be neglected.

We further investigate the orders of the first and last term in (31). Here below are listed typical baseline values for the optical parameters of the head tissues at a wavelength of 800 [nm]. Except for the cerebrospinal fluid (CSF), these values are taken from [12]. The analysis of CSF has to be done with more caution. Indeed, it is commonly admitted that the diffusion approximation of RTE is much less precise in CSF than in the other tissues [19, 32]. This is mainly due to the small scale of the optical parameters which yields a large mean free path and consequently a large diffusion coefficient κ. However, it has been pointed out in [32, 27] that the subarachnoid space is not only filled with CSF but also contains thin filaments, the arachnoid trabeculae (AT), that connect the two inner meninges, arachnoid mater and pia mater. Taking into account these small scatterers by homogeneization yields the values in Table 2 for a proportion of $p = 15\%$ AT among CSF (see [27] for details) and attests that $\omega/c \ll \mu_a + \mu_s'$ in all tissues. This implies that the first term in (31) can be neglected.

Tissu	$\mu_a\ [mm^{-1}]$	$\mu'_s\ [mm^{-1}]$	$\mu_a + \mu'_s$	$\omega/c\ [mm^{-1}]$
scalp	0.018	1.9	1.918	0.0028
skull	0.016	1.6	1.616	0.0028
CSF/AT	0.0062	0.3122	0.3184	0.0028
grey matter	0.048	0.5	0.548	0.0028
white matter	0.037	1.0	1.037	0.0028

Table 2: Baseline values for optical parameters of the neonatal head at 800 nm [12]. Constant anisotropy factor $g = 0.9$ and refractive index $n = 1.33$ for all tissues. Pulsation $\omega = 2\pi f$ with modulation frequency $f = 10^8[Hz]$. Homogenization of CSF/AT with $p = 15\%$ AT among CSF [27].

2.2 The time-dependent diffusion approximation

The system resulting from (30)–(31) and dimensional analysis reads

$$\frac{i\omega}{c}\Phi(t,\mathbf{x}) + \nabla\cdot\mathbf{I}(t,\mathbf{x}) + \mu_a(t,\mathbf{x})\Phi(t,\mathbf{x}) = q_0(\mathbf{x}) \tag{32}$$

$$\frac{1}{3}\nabla\Phi(t,\mathbf{x}) + (\mu_a(t,\mathbf{x}) + \mu'_s(t,\mathbf{x}))\mathbf{I}(t,\mathbf{x}) = 0, \tag{33}$$

and implies that the photon flux $\mathbf{I}$ derives from the scalar potential Φ. Substituting $\mathbf{I}$ in (32) then yields the diffusion equation

$$-\nabla\cdot(\kappa\nabla\Phi) + \left(\mu_a + \frac{i\omega}{c}\right)\Phi = q_0,$$

where the diffusion coefficient $\kappa = \dfrac{1}{3(\mu_a + \mu'_s)}$ and the absorption coefficient μ_a are functions of time and space variables $(t,\mathbf{x})$. In order to take into account inner reflection at the boundary between the scalp and the exterior domain, a Robin-type boundary condition is prescribed on Γ [22]. Hence, the boundary problem of the diffusion approximation with time-harmonic light source and time-dependent optical parameters reads

$$\begin{cases} -\nabla\cdot(\kappa\nabla\Phi) + \left(\mu_a + \dfrac{i\omega}{c}\right)\Phi = q_0 & \text{in } (0,T)\times\Omega, \\ \Phi + A\kappa\partial_n\Phi = 0 & \text{on } (0,T)\times\Gamma. \end{cases} \tag{34}$$

Here, $A > 0$ is a scalar coefficient that depends on the refractive index (RI) mismatch between the biological tissue of RI n and the surrounding medium of RI n_a. A precise formula for A can be found in [11].

Problem (34) is well posed in the following sense:

Theorem 2.1. *Let μ_a and κ belong to $\mathcal{C}^0(0,T;L^\infty(\Omega))$ and assume that there are constants $\mu_{a,0} > 0$ and $\kappa_0 > 0$ such that*

$$\mu_a \geq \mu_{a,0} \text{ and } \kappa \geq \kappa_0\ \forall t\in[0,T],\ \text{a.e. on } \Omega. \tag{35}$$

Let $q_0 \in L^2(\Omega;\mathbb{C})$ and $A > 0$. Then, there is a unique solution $\Phi \in \mathcal{C}^0(0,T;H^1(\Omega;\mathbb{C}))$ such that for any $t\in[0,T]$

$$a_t(\Phi(t,\cdot),v) = \ell(v)\ \forall v\in H^1(\Omega;\mathbb{C}), \tag{36}$$

where

$$a_t(u,v) = \int_\Omega \kappa(t,\cdot)\nabla u\cdot\nabla\bar{v}\,d\mathbf{x} + \int_\Omega\left(\mu_a(t,\cdot) + \frac{i\omega}{c}\right)u\bar{v}\,d\mathbf{x} + \frac{1}{A}\int_\Gamma u\bar{v}\,ds \tag{37}$$

is a sesqui-linear form defined for fixed t on $H^1(\Omega;\mathbb{C})\times H^1(\Omega;\mathbb{C})$ and

$$\ell(v) = \int_\Omega q_0\bar{v}\,d\mathbf{x} \tag{38}$$

is an antilinear form on $H^1(\Omega;\mathbb{C})$.

Proof. Notice that the assumptions on the data μ_a, κ and A guarantee that the sesquilinear form $a_t(\cdot,\cdot)$ is continuous and coercive on $H^1(\Omega;\mathbb{C})$ for any $t \in [0,T]$ with constants independent from t. Since $q_0 \in L^2(\Omega;\mathbb{C})$, the antilinear form ℓ is time-independent and continuous on $H^1(\Omega;\mathbb{C})$. At fixed time t, there is thus a unique solution $\Phi(t,\cdot) \in H^1(\Omega;\mathbb{C})$, solution to (36) due to Lax-Milgram's lemma for complex Hilbert spaces. Continuity of the solution Φ with respect to time then follows from the continuity of the parameters. Indeed, let $(t_n)_{n\in\mathbb{N}}$ be a convergent sequence in $[0,T]$ such that $\lim_{n\to\infty} t_n = t^*$. Let $\Phi_n = \Phi(t_n,\cdot)$ and $\Phi^* = \Phi(t^*,\cdot)$ the corresponding solutions of (36) at t_n and t^*, respectively. Then, for any $v \in H^1(\Omega;\mathbb{C})$, we have

$$\begin{aligned} a_{t_n}(\Phi_n - \Phi^*, v) &= a_{t_n}(\Phi_n, v) - a_{t^*}(\Phi^*, v) + a_{t^*}(\Phi^*, v) - a_{t_n}(\Phi^*, v) \\ &= \ell(v) - \ell(v) + a_{t^*}(\Phi^*, v) - a_{t_n}(\Phi^*, v) \\ &\longrightarrow 0 \end{aligned}$$

as $n \to \infty$ since the coefficients κ and μ_a are continuous with respect to t. Then, we infer from the coercivity of $a_t(\cdot,\cdot)$ that

$$\|\Phi_n - \Phi^*\|_{1,\Omega} \leq \frac{1}{\alpha} \Re\left(a_{t_n}(\Phi_n - \Phi^*, \Phi_n - \Phi^*)\right) \longrightarrow 0$$

as $n \to \infty$ since the coercivity constant $\alpha = \min(\kappa_0, \mu_{a,0})$ is time-independent. □

3 A mathematical model for neurovascular coupling

Neurovascular coupling describes the hemodynamic response of the brain to the electrical activity of a group of neurons. Roughly speaking, the neuronal activity induces an increase of the cerebral blood flow in order to satisfy the increasing need of oxygen in the activated area. Changes in the concentrations of the involved chromophores oxyhemoglobin [HbO] and deoxyhemoglobin [Hb] imply changes in the optical parameters μ_a and μ_s'. In this section, we summarize the main compartments of neurovascular coupling, i.e. a model for neuronal activity based on the work of [29] and the balloon model [7, 8] for the hemodynamic response. The balloon model has been developed initially to describe the BOLD signal of functional MRI [7], but the correlations between the BOLD signal and the concentration of deoxyhemoglobin allow to use it in diffuse optical imaging, too. The full model allows to get the input moment $\mathbf{q}_m(t)$ in the source term (13) of the forward EEG problem (14) and the time-dependent absorption coefficient μ_a in the forward DOT problem (34) while explaining their link in neurovascular coupling. We start with the description of the neuronal model that yields the moment $\mathbf{q}_m(t)$.

3.1 The neuronal model

Neurons are responsible for transmitting information between brain cells, through electrical impulses and chemical signals. The neuron is composed by three parts, the soma or cell body, the dendrites and the axon. When a stimulus occurs, the dendrites transmit the message to the soma which generates an action potential under appropriate conditions. The action potential is in turn sent through the axon and arrives at the presynaptic neuronal membrane which is separated from the postsynaptic neuron by the synaptic cleft. The action potential induces the release of neurotransmitters into the synaptic cleft which passes the information to the postsynaptic neuron and creates the postsynaptic potential.

Here, we present the neuronal model as a system of coupled ordinary differential equations. At the neuron level, the membrane potentials ν_s and ν_d of the soma and the dendrite in presence of an input stimulus I_{stim} are solutions of the following differential equations:

$$C_m \frac{\mathrm{d}\nu_s}{\mathrm{d}t} = -I_{\text{s,tot}} + C_a(\nu_d - \nu_s) + I_{\text{stim}}, \tag{39}$$

$$C_m \frac{\mathrm{d}\nu_d}{\mathrm{d}t} = -I_{\text{d,tot}} + C_a(\nu_s - \nu_d), \tag{40}$$

where C_m is the specific membrane capacitance and C_a is a constant which depends on the properties of the neuron.

Voltage gated membrane currents and ionic concentrations

The total cross membrane currents $I_{*,\mathrm{tot}}$ ($* \in \{s, d\}$) in the soma (resp. dendrite) compartment are the sum of voltage dependent sodium (Na) and potassium (K) currents $I_{\mathrm{s,Ion}}$ (resp. $I_{\mathrm{d,Ion}}$) and sodium, potassium and chlore leak currents as well as sodium-potassium exchange currents. Except for the leak currents, the ionic cross membrane currents are modelled using the Goldman-Hodgkin-Katz (GHK) formula

$$I_{*,\mathrm{Ion}} = g_{*,\mathrm{Ion}} \frac{F\nu_*([\mathrm{Ion}]_{i,*} - \exp(-\nu_*/\Phi)[\mathrm{Ion}]_e)}{\Phi \exp(-\nu_*/\Phi)},\ \mathrm{Ion} \in \{\mathrm{Na}, \mathrm{K}\},\ * \in \{\mathrm{s}, \mathrm{d}\}, \tag{41}$$

where $g_{*,\mathrm{Ion}}$ is the channel specific conductance, $[\mathrm{Ion}]_{i,*}$ and $[\mathrm{Ion}]_e$ denote the (compartment specific) intra- and extracellular ionic concentrations, F is the Faraday constant, and $\Phi = RT/F$ depends on the universal gas constant R and the absolute temperature T.

The ionic exchange rates between the soma and the dendrite depend on the total ionic current and the flow of ions between the soma and the dendrite compartement which is assumed to be proportional to the difference of the ionic concentrations:

$$V_s \frac{\mathrm{d}[\mathrm{Ion}]_{i,s}}{\mathrm{d}t} = -C_s I_{\mathrm{s,Ion}} + C_{\mathrm{Ion}}([\mathrm{Ion}]_{i,d} - [\mathrm{Ion}]_{i,s}) \tag{42}$$

$$V_d \frac{\mathrm{d}[\mathrm{Ion}]_{i,d}}{\mathrm{d}t} = -C_d I_{\mathrm{d,Ion}} + C_{\mathrm{Ion}}([\mathrm{Ion}]_{i,s} - [\mathrm{Ion}]_{i,d}) \tag{43}$$

$$\frac{V_e}{V_s + V_d} \frac{\mathrm{d}[\mathrm{Ion}]_e}{\mathrm{d}t} = \frac{C_s}{V_s} I_{\mathrm{s,Ion}} + \frac{C_d}{V_d} I_{\mathrm{d,Ion}} \tag{44}$$

where V_s, V_d and V_e are respectively the volume of the soma, the dendrite and the extracellular space, and C_s, C_d and C_{Ion} are constants depending on the neuron and the ion under consideration.

The ionic currents given by the GHK-formula (41) travel across voltage gated ionic channels. Each channel has a conductance $g_{*,\mathrm{Ion}} = m^p_{*,\mathrm{Ion}} h^q_{*,\mathrm{Ion}} \bar{g}_{\mathrm{Ion}}$, product of an ion-specific maximum conductance $\bar{g}_{\mathrm{Ion}}$ and a factor $m^p_{*,\mathrm{Ion}} h^q_{*,\mathrm{Ion}} \in [0, 1]$ which describes the fraction of active and inactive open channels. The variables $m_{*,\mathrm{Ion}}$ and $h_{*,\mathrm{Ion}}$ are solutions of a couple of differential equations

$$\frac{\mathrm{d}m_{*,\mathrm{Ion}}}{\mathrm{d}t} = \alpha_{m,*,\mathrm{Ion}}(\nu_*)(1 - m_{*,\mathrm{Ion}}) - \beta_{m,*,\mathrm{Ion}}(\nu_*) m_{*,\mathrm{Ion}}, \tag{45}$$

$$\frac{\mathrm{d}h_{*,\mathrm{Ion}}}{\mathrm{d}t} = \alpha_{h,*,\mathrm{Ion}}(\nu_*)(1 - h_{*,\mathrm{Ion}}) - \beta_{h,*,\mathrm{Ion}}(\nu_*) h_{*,\mathrm{Ion}}, \tag{46}$$

with opening and closing rates α and β depending on the membrane potential ν_*. The expressions for the rates of the different gating particles are usually obtained by experimental fitting [20, 40, 29].

Leak currents

The leak currents are given by Ohm's law,

$$I_{*,\mathrm{leak,Ion}} = \bar{g}_{\mathrm{Ion}}(\nu_* - E_{\mathrm{Ion}}) \tag{47}$$

where E_{Ion} denotes the ion-specific potential at rest.

Sodium-potassium exchange currents

The coupling between the neuronal and the vascular compartment is realized by the sodium-potassium exchange pump which aims to balance the ionic concentrations between the intra- and extracellular space. These pumps are present as well in the soma as in the dendrite compartment. The pump moves out three intracellular sodium ions and two extracellular potassium ions:

$$I_{*,\mathrm{Na,pump}} = 3I_{*,\mathrm{pump}}, \tag{48}$$
$$I_{*,\mathrm{K,pump}} = -2I_{*,\mathrm{pump}}, \tag{49}$$

where the total current $I_{*,\mathrm{pump}}$ due to the Na/K-exchange pump is given as the product of a function $\gamma_{1,*}$ depending on the concentrations of intracellular sodium and extracellular potassium and a function $\gamma_{2,*}$ depending on the tissue oxygen concentration $[O_2]$,

$$I_{*,\mathrm{pump}} = I_{\max}\gamma_{1,*}\left([K]_e, [Na]_{*,i}\right)\gamma_{2,*}\left([O_2]\right). \tag{50}$$

Expressions for $\gamma_{1,*}$ and $\gamma_{2,*}$ can be found in [29].

In turn, the variation of oxygen concentration $[O_2]$ depends on the oxygen supply and consumption, and satisfies the differential equation

$$\frac{\mathrm{d}[O_2]}{\mathrm{d}t} = J\frac{[O_2]_b - [O_2]}{[O_2]_b - [O_2]_0} - M. \tag{51}$$

Here, J is the rate of change in oxygen concentration, $[O_2]_b$ and $[O_2]_0$ are, respectively, the steady state and baseline oxygen concentration, and $M = M([O_2], [\mathrm{K}]_e, [\mathrm{Na}]_{i,s}, [\mathrm{Na}]_{i,d})$ denotes the cerebral metabolic rate of oxygen ($\mathrm{CMRO_2}$) which accounts for variation in time of the oxygen consumption after stimulation due to the exchange pump and other processes [29].

3.2 The vascular compartment

One of the most popular models to describe the dynamics of the biomechanical and metabolic quantities involved in brain activation is the balloon model [7, 8]. It consists of two coupled differential equations for the concentration of deoxygenated hemoglobin [Hb] and the cerebral blood volume CBV of the venous compartment:

$$\frac{\mathrm{d}[\mathrm{Hb}]}{\mathrm{d}t} = \frac{1}{\tau_0}\left(\frac{M}{M_0} - \frac{[\mathrm{Hb}]}{\mathrm{CBV}}f_{\mathrm{out}}\right), \tag{52}$$
$$\frac{\mathrm{dCBV}}{\mathrm{d}t} = \frac{1}{\tau_0}\left(\frac{\mathrm{CBF}}{\mathrm{CBF}_0} - f_{\mathrm{out}}\right). \tag{53}$$

Here, τ_0 is the mean transit time at rest, i.e. the time that a given blood volume stays in the capillary circulation, and M_0 and CBF_0 are equilibrium values for the metabolic rate of oxygen M and the cerebral blood flow CBF, respectively. The cerebral blood flow in the arterioles of the vascular compartment is of Poiseuille type,

$$\mathrm{CBF} = \mathrm{CBF}_0\frac{R^4}{R_0^4} \tag{54}$$

where R is the radius of the arterioles and R_0 is the corresponding steady state value. The outgoing flow f_{out} is related to the blood volume CBV by

$$f_{\mathrm{out}} = \mathrm{CBV}^{\frac{1}{d}} + \tau\frac{d\mathrm{CBV}}{dt} \tag{55}$$

with empirical constants d and τ.

3.3 The complete differential system

In summary, we get a system of ordinary differential equations

$$\frac{\mathrm{d}U}{\mathrm{d}t} = \mathcal{F}(U) \tag{56}$$

which has to be completed by initial values $U(0) = U_0$. The vector U of unknowns can be split into two parts, on the one hand the neuronal part U_{neuron} which contains the membrane potentials ν_s and ν_d, the intra- and extracellular ionic concentrations $[\text{Ion}]_{i,*}$ and $[\text{Ion}]_e$ and finally the gating variables m and h, on the other hand the hemodynamic part U_{hd} containing the concentrations of oxygen and deoxygenated hemoglobin $[\text{O}_2]$ and [Hb] as well as the cerebral blood volume CBV. The right hand side of (56) may also be split into a vector $\mathcal{F}_{\text{neuron}}$ and $\mathcal{F}_{\text{hd}}$ but due to neurovascular coupling, $\mathcal{F}_{\text{neuron}}$ acts on U_{neuron} as well as on $[\text{O}_2]$ through the presence of the exchange pump current $I_{*,\text{pump}}$, whereas $\mathcal{F}_{\text{hd}}$ acts on U_{neuron} as well as on U_{hd} since the metabolic rate of oxygen M depends on the ionic concentrations $[\text{K}]_e$ and $[\text{Na}]_{i,*}$. Thus, system (56) reads

$$\frac{\mathrm{d}}{\mathrm{d}t}\begin{pmatrix} U_{\text{neuron}} \\ U_{\text{hd}} \end{pmatrix} = \begin{pmatrix} \mathcal{F}_{\text{neuron}}(U_{\text{neuron}}, [O_2]) \\ \mathcal{F}_{\text{hd}}(U_{\text{neuron}}, U_{\text{hd}}) \end{pmatrix}. \tag{57}$$

Notice that the full system of differential equations described in [28, 29] contains other compartments than the two mentioned here, as for example astrocyte.

3.4 The time-dependent source term of the forward EEG-problem

The post-synaptic current

In response to an action potential ν_s (i.e. a presynaptic spike), neurotransmitters are released at the presynaptic terminal. These neurotransmitters then move into the synaptic cleft and bind with receptors in the postsynaptic neuron, opening ion channels. This movement of ions across the neuronal membrane generates a postsynaptic current I_{post} which is given by

$$I_{\text{post}}(t) = g(t)(\nu_{\text{post}}(t) - \nu_{\text{rev}}). \tag{58}$$

Here, the conductance $g(t)$ depends on the presynaptic neuron, ν_{post} is the potential accross the postsynaptic membrane, and ν_{rev} is a (constant) reversal potential the value of which depends on the neurotransmitter.

There are different types of neurotransmitters and the model will depend on which neurotransmitter we consider. Here, we focus on a single channel model which is valid e.g. for AMPA or GABA_A which are, respectively, excitatory or inhibitory neurotransmitters. As before, we express the conductance as a maximum conductance $\bar{g}$ and a factor between 0 and 1 modeling the proportion of open channels. Thus, we have $g(t) = \bar{g}s(t)$ in (58) where s is obtained by solving the differential equation [13]

$$\frac{\mathrm{d}s}{\mathrm{d}t} = K_1[T](1 - s) - K_2 s, \tag{59}$$

with K_1, K_2 two constants that depend on the neurotransmitter and $[T]$ the concentration of neurotransmitters in the synaptic cleft. We use a relationship between $[T]$ and ν_s from [13] according to which $[T]$ is given by

$$[T](\nu_s) = \frac{T_{max}}{1 + \exp(-(\nu_s - V_T)/K_p)}, \tag{60}$$

where T_{max} is the maximum concentration of transmitters in the synaptic cleft, V_T the value at which the concentration is halfed, K_p models the steepness and ν_s is the presynaptic action potential, given by the resolution of (56).

Finally, the corresponding postsynaptic current is then given by the right hand side of (58) where the postsynaptic potential is taken as the membrane potential ν_d in the dendrites.

The time-dependent current dipolar moment

It is commonly admitted that EEG signals result from the sum of postsynaptic currents generated by a large amount of synchronized pyramidal neurons with similar orientiations. The above analysis describes potentials and currents at the neuron level.

The source term of the time-dependent forward EEG problem (14) is the divergence of the source current density $\mathbf{j}^p$ which in turn is a dipolar moment $\mathbf{q}$ multiplied by a Dirac delta δ_S if the active area of the brain at time t is localized at a single position S. The moment $\mathbf{q}$ depends on the postsynaptic current I_{post}, a length scale Δs and the number N_{syn} of synchronized neurons,

$$\mathbf{j}^p = \mathbf{q}(t) \cdot \delta_S = N_{\text{syn}} I_{\text{post}}(t) \Delta s \, \mathbf{e}(t) \cdot \delta_S, \tag{61}$$

where $\mathbf{e}(t) \in \mathbb{R}^3$ is a unit vector describing the orientation of the neurons at time t. The solution u of (14) then models the spatial distribution in the head of the postsynaptic potential generated by the neuronal current I_{post} at S_m over a time interval $(0, T)$.

The order of magnitude of $\mathbf{j}^p$ is of $10[nA.m^{-2}]$ for the following data

$$N_{\text{syn}} = 10^6, \; I_{\text{post}} \approx 10[pA], \; \Delta s = 1[\text{mm}].$$

The corresponding order of magnitude of the simulated potential u at the electrodes is about $10[\mu V]$ which is consistent with experimental data (cf. e.g. [4]).

3.5 Time-dependent optical parameters

Contrary to [29], we are not interested here in the BOLD signal, but in the concentrations of deoxy- and oxyhemoglobin $[\text{Hb}]_N$ and $[\text{HbO}_2]_N$ which we assume normalized by their (initial) values at rest. [Hb] is part of the vector of unknowns of system (56). $[\text{HbO}_2]_N$ can be obtained by the formula

$$[\text{HbO}_2]_N = [\text{HbT}]_N - [\text{Hb}]_N + 1 \tag{62}$$

where the total normalized concentration of hemoglobin $[\text{HbT}]_N$ is given by

$$[\text{HbT}]_N = \frac{[\text{Hb}]_N \, \text{CBF}_N}{M_N}, \tag{63}$$

with normalized cerebral blood flow CBF_N and normalized change of oxygen consumption M_N.

The main chromophores contributing to absorption in the biological tissues of the brain are deoxy- and oxyhemoglobin as well as water. The absolute absorption coefficient at rest can therefore be related to the concentrations of the chromophores by

$$\mu_{a,0} = \mu_{a,\text{water}} P_{\text{water}} + \alpha_{\text{Hb}} [\text{Hb}]_0 + \alpha_{\text{HbO}_2} [\text{HbO}_2]_0, \tag{64}$$

where P_{water} is the proportion of water in the cortex, and α_{Hb} and α_{HbO_2} are the specific extinction coefficients of Hb and HbO_2 [23]. Changes in deoxy- and oxyhemoglobin concentrations during cerebral activation lead to the modification of $\mu_{a,0}$ which is expressed in terms of the time-dependent normalized concentrations $[\text{Hb}]_N$ and $[\text{HbO}_2]_N$:

$$\Delta\mu_a(t) = \alpha_{\text{Hb}} [\text{Hb}]_0 \left([\text{Hb}]_N(t) - 1 \right) + \alpha_{\text{HbO}_2} [\text{HbO}_2]_0 \left([\text{HbO}_2]_N(t) - 1 \right). \tag{65}$$

The effect of cerebral activity on the scattering coefficient μ_s is less documented and will be neglected here.

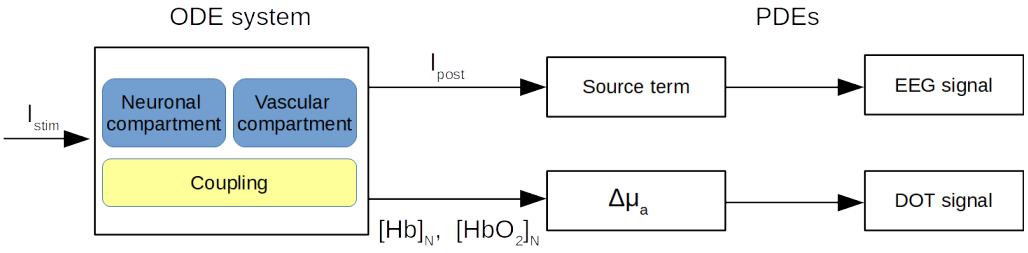

Figure 2: The full pipeline for simulation of co-registered EEG- and DOT-signals with a simplified representation of the different compartments of the ODE system.

4 Numerical simulation of co-registered EEG/DOT signals

In this section, we explain the numerical pipeline from an input stimulation current up to simulated co-registered EEG/DOT signals at the electroptodes according to Figure 2. Electroptodes are a medical device which allows to monitor simultaneously the neuronal and vascular activities of the brain [5].

We provide numerical simulations on a realistic head model of a healthy fullterm newborn obtained from coregistration of MR and CT images of the Amiens' hospital database (courtesy GRAMFC, INSERM U1105, Amiens, France (H. Azizollahi [5])). The model distinguishes between four tissues: brain, CSF, skull, ~~fontanels~~ and scalp. Table 3 summarizes the mesh parameters. Tables 1 and 2 give respectively the conductivity σ and the optical parameters $\mu_{a,0}$ and μ_s' of the tissues.

Nodes	Tetrahedra	h_{min} [m]	h_{max} [m]	diameter [m]
108 669	590 878	$3.4\ 10^{-4}$	$14\ 10^{-3}$	0.12

Table 3: Characteristics of the realistic head mesh.

Synthetic measurements are observed at $L = 8$ pointwise electroptodes $\{\mathbf{e}_\ell\}_{\ell=1}^{L}$ situated in different regions of the scalp on the boundary Γ. In Figure 3 (left), one distinguishes the electroptodes e_3 and e_5 situated respectively in the frontal and central area as well as e_2 and e_8 which are placed above the left hemisphere. We numerically simulate the measured EEG/DOT signals at electroptodes during the observation time interval $[0, T]$, with $T = 150$ms. We consider a single dipolar source point S below the electroptode e_2 and a moment $\mathbf{q}(t)$ directed normally to the brain/LCS interface (Figure 3 middle and right). We assume that the changes $\Delta\mu_a(t)$, given by (65), of the absorption parameter $\mu_{a,0}$ (at rest) are located in a ball $B_r(S)$ of radius $r = 1.2$cm and center S (see Figure 4). The volume of the ball represents 1.6% of that of the brain. We thus model a small and localized perturbation (in space) of the absorption coefficient caused by changes in deoxy- and oxyhemoglobin concentrations in the area of the electrical activity.

The method consists first in solving the complete system (56) of differential equations which, recall, models the neurovascular coupling at the neuron level. To this end, we apply the *ode15s* stiff solver with a variable step of Matlab [38]. Indeed, we need to simulate phenomena that occur at different time scales. The neuronal activity takes a few milliseconds and can show strong variations. The vascular part is characterized generally by a smooth behaviour along a period of several seconds. An order of 10000 time steps $(t_k)_{1\leq k\leq M}$ is required to obtain accurate results.

Simulations at the neuron level. We first analyse the link between the input stimulus I_{stim} and the output of the postsynaptic current I_{post} on the one hand and variations in the normalized concentrations $[\text{Hb}]_N$ and $[\text{HbO}_2]_N$ of deoxy- and oxyhemoglobin on the other. The model parameters are those of the neurotransmitter GABA_A. In Figure 5, we present the coupling between I_{post} and the variations of $[\text{Hb}]_N$ and $[\text{HbO}_2]_N$ for a rectangular pulse

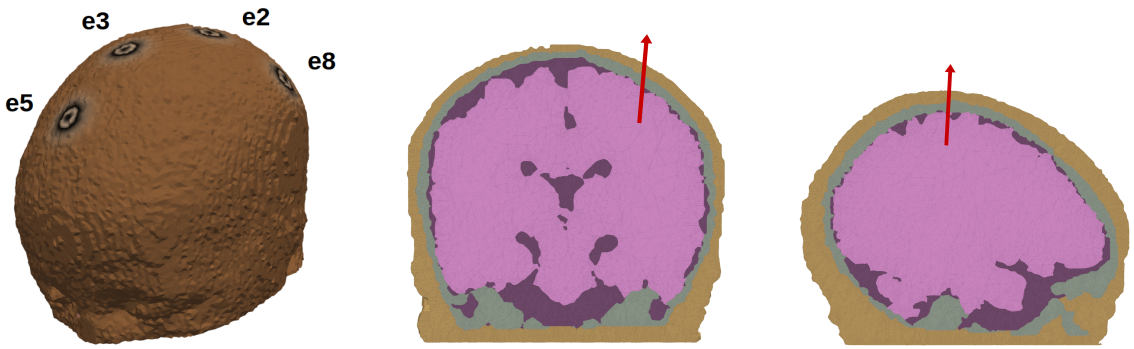

Figure 3: Position of the electroptodes (left). Frontal and sagittal view of position and orientation of the source.

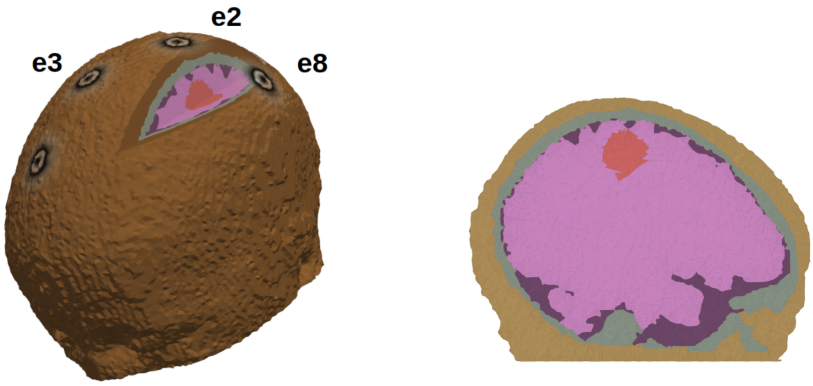

Figure 4: Localization in the brain of the perturbation in the absorption coefficient.

stimulation I_{stim} with amplitude $I_{\text{stim,max}} = 22[mA]$ which occurs during 1s in the time interval $[100, 101]$. We may notice that the most significant electrical activity is limited to the stimulation interval whereas an increase in $[\text{HbO}_2]_N$ and a symmetrical decrease in $[\text{Hb}]_N$ arise a few seconds after the neural activity.

We next study the influence of the stimulation current on the postsynaptic current and the hemodynamic concentrations. In Figure 6, we present I_{post} and the variations of $[\text{Hb}]_N$ and $[\text{HbO}_2]_N$ for a rectangular pulse stimulation I_{stim} with different amplitudes, $I_{\text{stim,max}} = 22[mA]$ (left column) and $I_{\text{stim,max}} = 19[mA]$ (middle). We notice that the amplitude of the stimulation pulse influences the spike density of the postsynaptic current. Results in the right column of Figure 6 correspond to an input stimulus I_{stim} containing two rectangular pulses (the first one of amplitude $I_{\text{stim,max}} = 22[mA]$ and the second $I_{\text{stim,max}} = 19[mA]$). The postsynaptic current has two periods of spikes, associated to the two pulses, with a higher density for the first one. One may notice that the global behavior of the hemodynamic response (lower line of Figure 6) is the same for the three configurations.

We have numerically exhibited the neurovascular coupling at the neuron level. In the next step, we are going to simulate the corresponding EEG/DOT measurements at the electroptodes. The EEG and DOT problems are solved simultaneously with input data obtained from system (56).

EEG signals. We compute the postsynaptic current $I_{\text{post}}(t_k)$ from (58) (see Section 3.4) and deduce the time-dependent source term F of the forward EEG model (14). We solve problem (14) by the subtraction approach and use the finite element method with Lagrange-$\mathbb{P}_1$ elements implemented in FreeFem++ [18] to compute the regular potentials $w_m^{(i)}$, $i \in \{1, \ldots, d\}$, solution to the variational formulation (21). Notice, that $w_m^{(i)}$ is time-independent in the present context of static source positions. Then, the potential u is

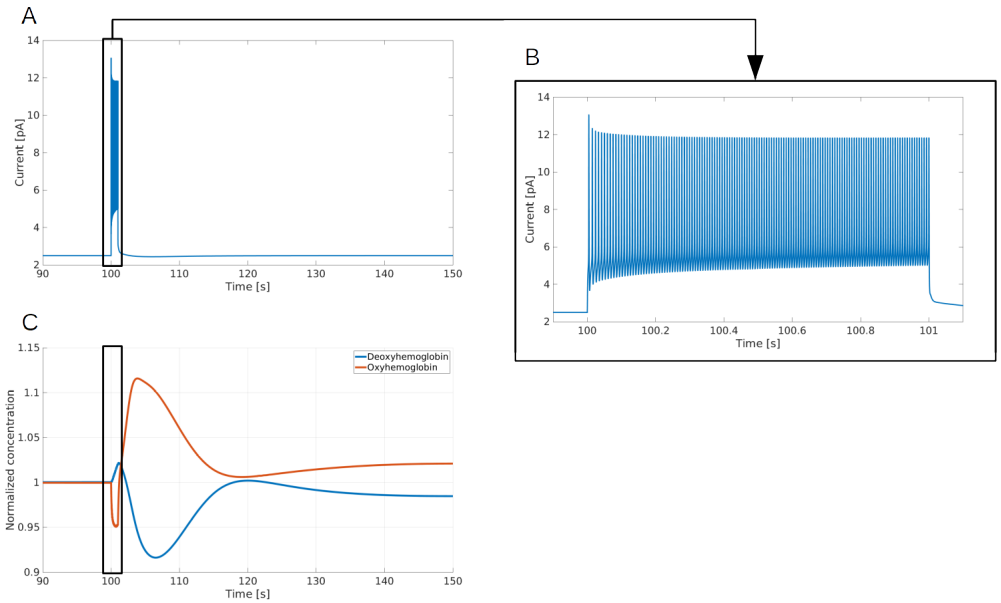

Figure 5: A: Simulated postsynaptic current I_{post} for a rectangular pulse stimulation of amplitude $I_{\text{stim,max}} = 22[mA]$ between 100 and 101$[s]$. B: Zoom of I_{post} to the interval $[100, 101]$. C: Normalized concentrations in deoxy- and oxyhemoglobin for the same stimulation.

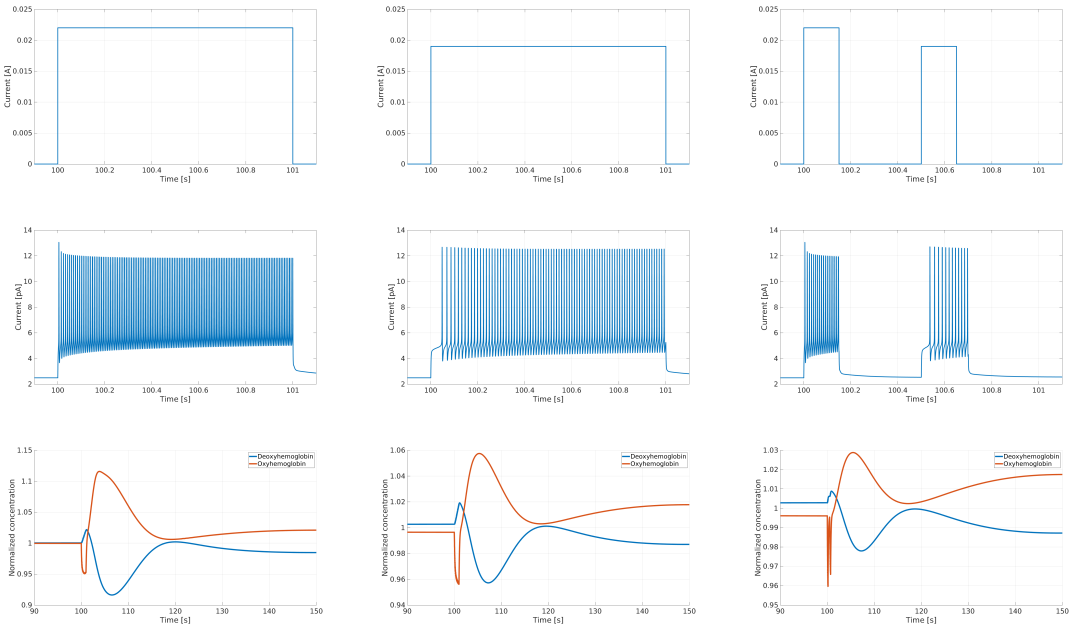

Figure 6: Simulated postsynaptic currents I_{post} (middle line, zoom on interval $[100, 101]$) and normalized concentrations of deoxy- and oxyhemoglobin (lower line) for different stimulation currents (upper line): rectangular pulse with amplitude $I_{\text{stim,max}} = 22[mA]$ (left) and $I_{\text{stim,max}} = 19[mA]$ (middle), two rectangular pulses of amplitudes $22[mA]$ and $19[mA]$ (right).

computed by linear combination from (22) and EEG measurements are given by

$$U_{k,\ell} = u(t_k, \mathbf{e}_\ell), \;\; k = 1, \ldots, K, \;\; \ell = 1, \ldots, L. \tag{66}$$

where K is the number of time steps. Due to the Neumann boundary condition, the solution u is determined up to an additive constant only. In Section 1, we considered the subspace of functions in $H^1(\Omega)$ with vanishing mean value to get uniqueness of the solution. In practice, the absolute potential cannot be measured by EEG and the measured

voltage is the difference between the potential at electroptode $\mathbf{e}_\ell$ and the potential at a reference electroptode. Numerically, we therefore impose a Dirichlet boundary condition on a single node of the mesh to fix the constant. Since the singularity of the potential u is taken into account exactly in the subtraction approach, the discretization error is given by the error on the regular potential. We refer to [6] for a detailed error analysis.

DOT signals. Concerning the vascular part, the resolution of system (56) allows the computation of the variation $\Delta\mu_a$ at time t_k from formula (65) (see Section 3.5) and the perturbed absorption coefficient is given by

$$\mu_a(t_k, \mathbf{x}) = \mu_{a,0}(t_k, \mathbf{x}) + \Delta\mu_a(t_k)\chi_{B_r(S)}(\mathbf{x}),$$

where χ is the characteristic function of the perturbation $B_r(S)$ in the brain. The light source q_0 is modeled as a Gaussian function

$$q_0(\mathbf{x}) = A_s \exp\left(-\frac{\|\mathbf{x} - \mathbf{x}_s\|}{2\sigma_s^2}\right)$$

where $\sigma_s = 5 \times 10^{-3}$ fixes the beam diameter and the amplitude is set to $A_s = (2\pi\sigma_s)^{-1}$. $\mathbf{x}_s$ is the center of the source which should be located at a distance $\delta \sim 1/\mu_s'$ away from the surface Γ in order to justify an isotropic source term. We solve problem (34) by means of Lagrange-$\mathbb{P}_1$ finite elements implemented in FreeFem++ on a coarsened time grid. This is numerically justified since variation in time for DOT arises at a larger time scale than in EEG, and allows to reduce the computational cost for the DOT problem. We normalize the photon density ϕ with respect to the reference configuration with no perturbation, i.e $\mu_a(t_k, \mathbf{x}) = \mu_{a,0}$. DOT measurements are thus expressed by

$$\phi_{k,\ell} = \frac{|\phi(t_k, \mathbf{e}_\ell)|}{|\phi_0(t_k, \mathbf{e}_\ell)|}, \ k = 1, \dots, K', \ \ell = 1, \dots, L,$$

where ϕ_0 is the solution of the DOT problem (34) with piecewise constant absorption coefficient $\mu_{a,0}$ and $K' \ll K$ is the number of reduced time steps. Baseline values for $\mu_{a,0}$ and μ_s' are those from Table 2.

In Figure 7, we report EEG/DOT-measurements associated with the rectangular pulse stimulation I_{stim} of amplitude $I_{\text{stim,max}} = 22[mA]$. According to formula (22), the electric potential u depends linearly on I_{post}. Thus, EEG measurements have the same temporal behavior than I_{post} (see Figure 5). Spikes are visible between $t = 100[s]$ and $t = 101[s]$ whereas the amplitude differs with respect to the position of the electrode. Electroptode e_2, which is located near the brain source S, records the most important changes in both the electric potential and the photon density. We observe that the simulated EEG and DOT measurements are correlated in time. These numerical results illustrate the neurovascular coupling and are consistent with clinical observations [36].

5 Conclusion

In this paper, we have developed and analysed a mathematical model for simulating co-registered EEG and DOT measurements. It combines a non-linear system of differential equations which models the neurovascular coupling at the neuron level, and PDE-based models for EEG and DOT that allow to compute signals at the electroptodes on the scalp. To this end, we have introduced evolution in time into the standard EEG and DOT models and justified the time-dependent models *via* a dimensional analysis. Existence and uniqueness results in appropriate vector spaces attest the well-posedness of both models. We have detailed the pipeline from the input stimulation of cerebral activity up to the co-registered EEG/DOT signals. Numerical results on a three-dimensional realistic head model illustrate the electric potential and hemodynamic changes occurring from neurovascular coupling. Up to the best of our knowledge, this is the first contribution

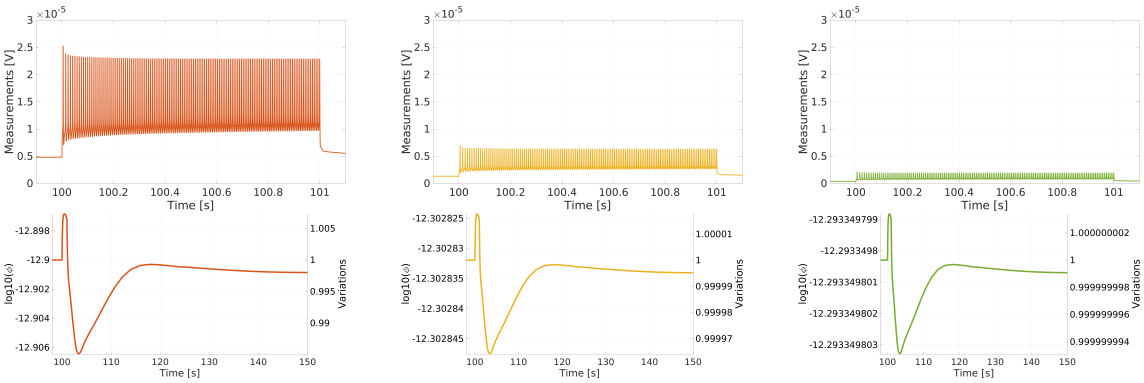

Figure 7: Simulation of co-registered EEG and DOT signals at electroptodes e_2 (left), e_3 (middle) and e_5 (right) for a rectangular pulse stimulation of $I_{\text{stim,max}} = 22[mA]$. Upper line: electric potential u (zoom on interval $[100, 101]$). Lower line: photon density Φ (in $\log_{10}$).

for modeling coupled EEG and DOT signals by solving both ODEs and PDEs. The generalization to other ionic models that provide both the postsynaptic current and the concentrations of deoxy- and oxyhemoglobin is straightforward.

Co-registered EEG/DOT signals give valuable information to clinicians for a deepful understanding of brain disorders. The derivation of a EEG/DOT forward model is therefore an essential preliminary step to the resolution of the corresponding inverse problem which consists in reconstructing simultaneously the location of electric sources and the optical parameters in the brain.

References

[1] S.R. Arridge, Optical tomography in medical imaging, Inverse Problems, 15(2):R41, 1999.

[2] S.R. Arridge, J.C. Schotland, Optical tomography: forward and inverse problems, Inverse Problems , **25**(12) (2009): 123010.

[3] A. Aubert, R. Costalat, A model of the coupling between brain electrical activity, metabolism, and hemodynamics: application to the interpretation of functional neuroimaging, Neuroimage **17** (2002), 1162–1181.

[4] H. Aurlien, I.O. Gjerde, J.H. Aarseth, G. Eldøoen, B. Karlsen, H. Skeidsvoll, N.E. Gilhus. EEG background activity described by a large computerized database. Clin. Neurophysiol. **115** (2004), 665–673. doi: 10.1016/j.clinph.2003.10.019.

[5] H. Azizollahi, A. Aarabi, F. Wallois, Effects of Uncertainty in Head Tissue Conductivity and Complexity on EEG Forward Modeling in Neonates, Hum. Brain Mapp. **37**(10) (2016), 3604–22.

[6] H. Azizollahi, M. Darbas, M.M. Diallo, A. El Badia, S. Lohrengel, EEG in neonates: forward modeling and sensitivity analysis with respect to variations of the conductivity, Math. Biosci. Eng. **15** (2018), 905–932.

[7] R.B. Buxton, E.C. Wong, L.R. Frank, Dynamics of blood flow and oxygenation changes during brain activation : The balloon model, Magnetic Resonance in Medicine **39**(6) (1998), 855–864.

[8] R.B. Buxton, K. Uludag, D.J. Dubowitz, T.T. Liu, Modeling the hemodynamic response to brain activation. NeuroImage **23** (2004), S220–S233.

[9] M. Chalia *et al*, Hemodynamic response to burst-suppressed and discontinuous electroencephalography activity in infants with hypoxic ischemic encephalopathy, Neurophotonics 3.3 (2016): 031408-031408.

[10] M. Darbas, S. Lohrengel, Review on mathematical modelling of electroencephalography (EEG), Jarhesber. Dtsch. Math.-Ver. **121** (2019), 3–39.

[11] H. Dehghani, M. E. Eames, P. K. Yalavarthy, S. C. Davis, S. Srinivasan, C. M. Carpenter, B. W. Pogue, K. D. Paulsen, Near infrared optical tomography using NIRFAST : Algorithm for numerical model and image reconstruction, Communications in Numerical Methods in Engineering, **25**(6) (2009), 711–732.

[12] M. Dehaes, K. Kazemi, M. Pélégrini-Issac, R. Grebe, H. Benali, F. Wallois. Quantitative Effect of the Neonatal Fontanel on Synthetic Near Infrared Spectroscopy Measurements, Human brain Mapping. 2013; **34**:878–889.

[13] A. Destexhe, Z. F. Mainen, T. J. Sejnowski, Synthesis of models for excitable membranes, synaptic transmission and neuromodulation using a common kinetic formalism. J. Comput. Neurosci., 1:195-230, 1994.

[14] A. El Badia, T. Ha-Duong, An inverse source problem in potential analysis, Inverse Problems **16** (2000), 651–663.

[15] O. Faugeras, F. Clément, R. Deriche, R. Keriven, T. Papadopoulo, J. Roberts, T. Viéville, F. Devernay, J. Gomes, G. Hermosillo, P. Kornprobst, D. Lingrand, The inverse EEG and MEG problems: The adjoint state approach I: The continuous case Inria version 1, 1999, hal.inria.fr/docs/00/07/71/12/PDF/RR-3673.pdf

[16] C. Gabriel, Compilation of the Dielectric Properties of Body Tissues at RF and Microwave Frequencies (1996), doi:10.21236/ada303903.

[17] A. Gallagher, F. Wallois, H. Obrig, Functional near-infrared spectroscopy in pediatric clinical research: Different pathophysiologies and promising clinical applications, Neurophotonics. 2023 **10**(2):023517.

[18] F. Hecht, New development in FreeFem++. J. Numer. Math. **20**(3-4) (2012), 251–266.

[19] A.H. Hielscher, R.E. Alcouffe, R. L. Barbour, Comparison of finite-difference transport and diffusion calculations for photon migration in homogeneous and heterogeneous tissues, Phys. Med. Biol. 1998; **43** (1998):1285–1302.

[20] A.L Hodgkin, A.F. Huxley, A quantitative description of membrane current and its application to conduction and excitation in nerve. The Journal of Physiology, **117** (1952) doi: 10.1113/jphysiol.1952.sp004764.

[21] IT'IS Foundation, https://itis.swiss/virtual-population/tissue-properties/database/dielectric-properties/, visited on March 4th, 2022.

[22] J. P. Kaipio, E. Somersalo, Statistical and Computational Inverse Problems, **160**, Applied Mathematical Sciences, Springer, New York, NY, 2005.

[23] L. Kocsis, P. Herman, A. Eke, The modified Beer-Lambert law revisited. Physics in medicine and biology **51** (2006),N91–8.

[24] T. Koskela, G.S. Kendall, S. Memon, M. Sokolska, T. Mabuza, A. Huertas-Ceballos, S. Mitra, N. J. Robertson, J. Meek, K. Whitehead, Prognostic value of neonatal EEG following therapeutic hypothermia in survivors of hypoxic-ischemic encephalopathy, Clinical Neurophysiology, **132**(9) (2021), 2091–2100.

[25] C. Lee, R. Cooper, T. Austin, Diffuse optical tomography to investigate the newborn brain, Pediatr Res **82** (2017), 376–386.

[26] S. Lew, D.D. Sliva, M. Choe, P.E. Grant, Y. Okada, C.H. Wolters, M.S. Hämäläinen, Effects of sutures and fontanels on MEG and EEG source analysis in a realistic infant head model, Neuroimage **76** (2013), 282–293. doi:10.1016/j.neuroimage.2013.03.017

[27] S. Lohrengel, F. Mahmoudzadeh, F. Oumri, S. Salmon, F. Wallois, A homogenized cerebrospinal fluid model for diffuse optical tomography in the neonatal head, Int J Numer Method Biomed Eng. **38**(1) (2022) doi: 10.1002/cnm.3538.

[28] E.J. Mathias, Computational modelling of neurovascular coupling and the BOLD signal, PHD, Univ. Canterbury, 2017.

[29] E.J. Mathias, A. Kenny, M.J. Plank, T. David, Integrated models of neurovascular coupling and BOLD signals : Responses for varying neural activations. NeuroImage **174** (2018) 69–86.

[30] B. Montcel, R. Chabrier, P. Poulet, Time-resolved absorption and hemoglobin concentration difference maps: a method to retrieve depth-related information on cerebral hemodynamics, Opt Express. 2006 Dec 11;14(25):12271-87. doi: 10.1364/oe.14.012271.

[31] M. Nourhashemi, M. Mahmoudzadeh, S. Goudjil, G. Kongolo, F. Wallois, Neurovascular coupling in the developing neonatal brain at rest, Human Brain Mapping (2020) **41**(2), 503–519.

[32] E. Okada, D.T. Delpy, Near-infrared light propagation in an adult head model. I. Modeling of low-level scattering in the cerebrospinal fluid layer, Appl. Optics. 2003;**42**(16):2906–2914.

[33] S. Pursiainen, F. Lucka, C.H. Wolters, Complete electrode model in EEG: relationship and differences to the point electrode model, Physics in Medicine & Biology, 2012.

[34] F. Rapetti, G. Rousseaux, On quasi-static models hidden in Maxwell's equations, Appl. Num. Math. **79** (2014), 92–106.

[35] J.M. Rennie, L.S. de Vries, M. Blennow, *et al*, Characterisation of neonatal seizures and their treatment using continuous EEG monitoring: a multicentre experience, Arch Dis Child Fetal Neonatal Ed 2019;**104**:F493-F501.

[36] N. Roche-Labarbe, F. Wallois, E. Ponchel, G. Kongolo, R. Grebe, Coupled oxygenation oscillation measured by NIRS and intermittent cerebral activation on EEG in premature infants, NeuroImage **36** (2007), 718–727, https://doi.org/10.1016/j.neuroimage.2007.04.002.

[37] N. Roche-Labarbe, B. Zaaimi, P. Berquin, A. Nehlig, R. Grebe, F. Wallois, NIRS-measured oxy- and deoxyhemoglobin changes associated with EEG spike-and-wave discharges in children, Epilepsia (2008) **49**(11), 1871-1880. doi: 10.1111/j.1528-1167.2008.01711.x.

[38] L. F. Shampine, M. W. Reichelt. The MATLAB ODE Suite. SIAM Journal on Scientific Computing. **18** (1997), 1-22.

[39] S.Sten, H. Podéus, N. Sundqvist, F. Elinder, M. Engström, *et al.*, A quantitative model for human neurovascular coupling with translated mechanisms from animals, PLOS Computational Biology **19**(1) (2023), e1010818.

[40] R.D. Traub, J.G.R. Jefferys, R. Miles, M.A. Whittington, K. Tóth, A branching dendritic model of a rodent CA3 pyramidal neurone, J. Physiol. **481** (1994), 79–95.

[41] J. Vorwerk, M. Clerc, M. Burger, C.H. Wolters, Comparison of boundary element and finite element approaches to the EEG forward problem. Biomed Tech (Berl). 2012

[42] F. Wallois, M. Mahmoudzadeh, A. Patil, R. Grebe, Usefulness of simultaneous EEG-NIRS recording in language studies, Brain Lang. **121**(2) (2012), 110-123.

[43] C.H. Wolters, H. Köstler, C. Möller, J. Härdtlein, L. Grasedyck, W. Hackbusch, Numerical mathematics of the subtraction method for the modelling of a current dipole in EEG source reconstruction using finite element head models, SIAM J. Sci. Comput. **30** (2007), 24–45.